An analogue-conditioned multi-satellite framework for daily precipitation reconstruction

Adrian Huerta[1,2*], Roberto Serrano-Notivoli[3] and Stefan Brönnimann[1,2]

[1]Oeschger Centre for Climate Change Research, University of Bern, Hochschulstrasse 4, Bern, 3012, Switzerland.
[2]Institute of Geography, University of Bern, Hallerstrasse 12, Bern, 3012, Switzerland.
[3]Departamento de Geografia y Ordenación del Territorio, Instituto Universitario de Ciencias Ambientales (IUCA), Universidad de Zaragoza, Calle de Pedro Cerbuna 12, Zaragoza, 50009, Zaragoza, Spain.

*Corresponding author(s). E-mail(s): adrhuerta@gmail.com;

Abstract

Precipitation is a key component of the Earth system, yet remains difficult to reconstruct accurately due to its stochastic nature, physical drivers, and sparse observational coverage. Existing gridded datasets rely on trade-offs between station-based observations, satellite retrievals, and multi-source blending, often introducing inconsistencies and temporal limitations. Here, we present an analogue-conditioned multi-source daily precipitation reconstruction framework that integrates physically consistent analogue-pattern selection with spatial data fusion. By conditioning reconstruction on precipitation analogues, the framework enables the transfer of information across time, allowing satellite-era observations to inform historical reconstructions while preserving large-scale structure. Applied over Tropical South America, the method demonstrates robust performance across observational variants, climate regimes, and spatial scales, accurately reproducing precipitation magnitude and occurrence. The framework provides a unified approach from station to grid scale and reduces dependencies on blended datasets. It generates spatially coherent fields suitable for the analysis of extremes and long-term trends. This approach offers a flexible and scalable pathway for reconstructing high-resolution precipitation datasets in regions with limited observational coverage.

Keywords: precipitation, analogue, spatial fusion model, satellite precipitation

1 Introduction

Precipitation is a fundamental hydrometeorological variable and the primary driver of the global water cycle, governing freshwater availability, ecosystem dynamics, and hydrological hazards such as floods and landslides [1–4]. Despite its central role, it remains one of the most challenging climate variables to estimate and reconstruct across spatial and temporal scales [3–7]. Unlike other atmospheric variables that vary more smoothly, precipitation is inherently intermittent and highly heterogeneous in space and time [4, 5]. Its formation arises from complex interactions among atmospheric dynamics, convection, and cloud microphysics, spanning multiple scales and involving nonlinear processes [8, 9]. These characteristics, combined with sparse and uneven observational coverage—particularly in high-altitude watersheds, complex terrain, and remote regions—make it difficult to obtain accurate, high-resolution precipitation fields using conventional station-based observations.

Existing precipitation datasets reflect fundamental trade-offs between accuracy and coverage [10]. Station-based observations provide high-accuracy point measurements but are often spatially sparse, temporally incomplete, and affected by inhomogeneities arising from sensor limitations or changes in gauge-network composition [11, 12]. In contrast, satellite-based precipitation products offer near-global coverage. Still, they are constrained by their temporal availability and by retrieval uncertainties and biases, particularly over complex terrain and convective regimes [9, 13]. To mitigate these limitations, many high-resolution precipitation products rely on multi-source blending approaches that combine observations, radar estimates, satellite retrievals, and reanalysis outputs through sequential processing or weighted averaging [5, 14–17]. However, such approaches typically do not provide independent reconstructions and may introduce error cross-correlations due to shared input data used for calibration or forcing [18]. Moreover, transitions between different model configurations, or the harmonization of multi-source inputs with distinct bias characteristics, can introduce artificial temporal discontinuities and inconsistencies, potentially biasing long-term hydroclimatic analyses [17, 19, 20].

Analogue-based approaches provide a physically grounded pathway for precipitation reconstruction by identifying historical patterns similar to a target state, thereby preserving coherent spatial structures without requiring extensive training data or event-specific simulations [21–23]. By leveraging past observations, these methods enable the transfer of information across space and time, offering a natural framework for reconstructing precipitation under data-limited conditions [24–27]. However, traditional implementations typically rely on single-metric similarity and deterministic selection criteria, limiting their ability to represent multiple plausible states or to integrate heterogeneous sources of information. Common similarity measures often fail to reconcile pattern structure with absolute magnitude, potentially leading to analogue selections that lack true physical resemblance to the target event [23, 25, 28]. In parallel, data-driven approaches, particularly deep and machine learning methods, can enhance local precipitation estimates by capturing complex nonlinear relationships among multi-source inputs and environmental predictors [9, 18, 29, 30]. However, these methods often require large, high-quality training datasets, limiting their applicability in regions with sparse observational coverage. Moreover, many such models operate as

"black boxes" and lack inherent mechanisms to enforce physical consistency, leading to unrealistic spatial patterns or inconsistencies in reconstructed precipitation fields [30]. Together, these limitations highlight the absence of a unified framework that combines the physical coherence of analogue methods with the flexibility and multi-source integration capabilities of data-driven approaches.

Here we present an Analogue-Conditioned Multi-Satellite Precipitation Reconstruction (AC-MSPR) framework that bridges these limitations (Figure 1). AC-MSPR is a hybrid data-driven approach in which physical pattern similarity—identified through precipitation analogues—guides a flexible statistical learning model to reconstruct daily precipitation at both point and gridded scales. The framework combines multi-criteria analogue-pattern selection, based on a Pareto-frontier approach, with spatial data fusion that integrates satellite precipitation, analogue-derived environmental features, and station observations. By conditioning the reconstruction on analogue relationships, AC-MSPR enables the transfer of information across time, allowing present-day satellite observations to inform historical reconstructions and, conversely, historical patterns to enhance the interpretation of recent data. This approach overcomes the temporal limitations of satellite datasets while preserving physically consistent large-scale precipitation structures. At the same time, the spatial data fusion component incorporates local observational constraints, improving the representation of fine-scale variability and extremes.

We evaluate AC-MSPR using the serially complete daily precipitation dataset for South America (SC-PREC4SA [12]), a newly developed observational dataset that provides multiple variants reflecting different levels of temporal completeness, consistency, and observational realism. This enables a systematic assessment of how data characteristics influence analogue selection and reconstruction performance. We demonstrate the framework over Tropical South America, a region characterized by strong hydroclimatic gradients and limited observational coverage [12, 31–33]. Through analyses of analogue selection behavior, spatial and temporal validation, and applications to precipitation extremes and trends, we therefore illustrate that AC-MSPR provides accurate, robust, and spatially consistent reconstructions across diverse climatic conditions.

2 Results

2.1 Illustrative reconstruction using AC-MSPR

To demonstrate the workflow and capabilities of the AC-MSPR framework, a representative reconstruction over Tropical South America for 10 January 1960 is presented (Figure 2). This example illustrates how multi-criteria analogue precipitation-pattern selection and spatial data fusion interact to generate spatially coherent and observation-constrained precipitation fields at a time when only a sparse network of field observations was available.

The reconstruction was anchored by station-based precipitation from the SC-PREC4SA dataset, which provides spatially sparse yet temporally complete observations (Figure 2a). This snapshot highlights the pronounced spatial heterogeneity of precipitation across the region and serves as the reference for both analogue selection and spatial data fusion.

First, the framework identified historical analogue precipitation patterns from satellite-based products (PDIR-now, IMERG-Early, and GSMaP_NRT). Candidate analogues were selected from the 1998–2021 period using a Pareto-frontier approach that jointly considers multiple similarity metrics, constrained to days with comparable seasonal and large-scale meteorological conditions (Figure 2b). This multi-objective selection avoided reliance on a single criterion and instead retained solutions that represent optimal trade-offs between overall agreement, extreme-event representation, and precipitation occurrence. These aspects were quantified using the refined index of agreement for all values (d_r) and extremes (d_r^{p90}), together with the Matthews correlation coefficient (MCC) (Figure 2c). The resulting set of analogue candidates (43 in this example) captured a range of plausible large-scale precipitation states, rather than a single optimal match, which is particularly important in regions with sparse and uneven observational coverage.

The final reconstruction step is shown in Figure 2d. For each selected analogue, precipitation fields were reconstructed using a spatial data fusion model that integrates satellite analogue patterns, analogue-derived cloud-based features (e.g., from the PATMOS-x dataset), and station observations. This step refined large-scale precipitation patterns by incorporating local observational constraints and spatial dependencies, thereby improving the representation of localized features while preserving spatial coherence. As a result, the reconstructed fields reproduce the main characteristics of the observed precipitation, including both broad-scale structures and regional variability. This was further supported by high performance across statistical metrics comparing gridded and station-based precipitation, including d_r, MCC, the modified Kling–Gupta efficiency (KGE''), and balanced accuracy ($BAcc$), for both magnitude and occurrence. Despite this overall high skill, individual analogue-based reconstructions exhibited distinct spatial variability, reflecting the range of analogue-conditioned precipitation states represented in the ensemble. Uncertainty arises from both the spatial data fusion model itself and the spread across analogue-based ensemble members. The framework naturally produced an ensemble of reconstructed fields by considering each analogue as an ensemble member; the ensemble median provides the best estimate, while the standard deviation quantifies reconstruction uncertainty.

Overall, this example highlights the complementary roles of analogue selection and spatial data fusion within the AC-MSPR framework. While analogue patterns provide physically consistent representations of large-scale precipitation structures, the spatial data fusion step adapts these patterns to local observations, resulting in accurate and spatially coherent precipitation reconstructions. The framework can be flexibly applied in both ensemble mode, which quantifies uncertainty, and deterministic mode based on a single representative analogue, where uncertainty is instead characterized by the spatial data fusion model error, enabling efficient large-scale applications. This dual capability underscores the adaptability of AC-MSPR across different use cases, from uncertainty-aware analyses to computationally efficient long-term reconstructions at different spatial resolutions.

2.2 Analogue-pattern selection insights in AC-MSPR

To assess the robustness of analogue selection within AC-MSPR, we evaluated its sensitivity to different observational data variants across Tropical South America, considering multiple characteristics of the analogue sets, including similarity, size, frequency by satellite precipitation product, and performance based on analogue metrics. In addition, we examined how these properties vary under large-scale climate conditions associated with different ENSO regimes (Figure 3).

Figure 3a shows the similarity between analogue sets derived from different SCPREC4SA variants, quantified using the Jaccard index. Overall, the degree of overlap varied substantially across observed variants, indicating that the underlying data characteristics influence analogue selection. In particular, the temporally complete (obs_bc) and temporally consistent (hmg_obs_bc) datasets exhibited relatively high similarity, with mean Jaccard values reaching up to 0.75. In contrast, the qc_obs dataset, which prioritizes observational realism but contains temporal gaps, showed considerably lower similarity with both obs_bc and hmg_obs_bc, with mean values around 0.25. These differences arise from variations in network completeness, as the changing station availability in qc_obs leads to distinct analogue pools, highlighting the role of data completeness and homogeneity in shaping the identification of similar precipitation patterns.

The distribution of analogue set sizes further illustrates the influence of observational constraints (Figure 3b). Variants with temporally complete records (obs_bc and hmg_obs_bc) yielded mean set sizes of approximately 45 analogues, with values ranging between 5 and 100. In contrast, qc_obs produced slightly larger analogue sets on average, with maxima reaching up to 120 analogues for certain dates. This increase can be attributed to the higher variability in station availability, whereby the changing observational network alters the spatial representativeness of the target field and enables a broader range of candidate analogues to satisfy the selection criteria. As a result, qc_obs effectively relaxes spatial constraints in some regions while emphasizing others, leading to larger but potentially less consistent analogue pools. These patterns reflect a trade-off between data availability and analogue specificity, with direct implications for reconstruction flexibility and uncertainty. Notably, from an ENSO perspective, analogue set sizes remain relatively stable across neutral, El Niño, and La

Niña conditions, indicating that extremely large-scale climate conditions exert limited influence on the number of selected analogues.

Regarding the satellite precipitation products, their relative contribution to the analogue sets exhibited distinct yet consistent patterns (Figure 3c). IMERG-Early and PDIR-Now showed slightly higher frequencies within the analogue pools ($\approx$ 30-45%), whereas GSMaP_NRT contributes less frequently ($\approx$ 20-35%). Notably, this distribution remained broadly consistent across observational variants and ENSO regimes, indicating a stable balance among satellite data sources within the Pareto-based selection framework. Such behavior reflects the ability of the Pareto-frontier approach to retain a diverse set of solutions that represent different trade-offs among performance metrics, rather than favoring a single dominant product.

Differences in analogue performance across satellite products are further illustrated in Figure 3d. GSMaP_NRT exhibited comparatively higher skill in representing overall precipitation, with mean d_r values around 0.65, while IMERG-Early and PDIR-Now show slightly lower performance for this metric. In contrast, IMERG-Early and PDIR-Now outperformed GSMaP_NRT in capturing precipitation extremes and occurrence, with d_r^{p90} and MCC values of approximately 0.45 and 0.35, respectively, whereas GSMaP_NRT showed reduced skill in these aspects. These results indicate that no single satellite product consistently outperforms the others across all performance dimensions and also support the relative contributions of the products.

Therefore, analogue selection within AC-MSPR does not converge toward a single preferred satellite product or precipitation skill metric, but instead dynamically integrates complementary strengths across datasets through a set of Pareto-optimal solutions. This behavior tends to remain robust across observational data variants, with only limited sensitivity to ENSO-driven climate variability. While differences between qc_obs and the temporally complete datasets (obs_bc and hmg_obs_bc) are evident in analogue set similarity and size, these do not translate into substantial changes in satellite product frequency or performance. The resulting ensemble of analogue patterns provides an implicit representation of uncertainty, capturing a range of plausible precipitation states consistent with both observations and satellite information. Together, these results highlight the ability of the multi-criteria selection framework to flexibly and coherently represent the complexity of precipitation processes without reliance on any single data source or metric.

2.3 Spatial-data fusion performance in AC-MSPR

The performance of the spatial data fusion component within AC-MSPR was evaluated using leave-one-out cross-validation in both space and time, considering multiple observational data variants under different ENSO regimes (Figures 4 and 5). For these evaluations, reconstructions were based on the best-performing analogue (highest mean of d_r, d_r^{p90}, and MCC) from the Pareto-selected set, rather than the ensemble median. While the ensemble approach provides an estimate of uncertainty, selecting a single representative analogue preserves event-specific spatial structures and avoids the smoothing effects associated with aggregation. This is particularly important for accurately representing extremes and localized precipitation features at the point/station scale.

As the analysis is conducted over Tropical South America, it provides insight into the robustness of the reconstruction framework in reproducing precipitation variability across highly heterogeneous environments, ranging from extremely arid to wet conditions, as seen by its ecological regions (Figure 1a and SI Section 1.1): Northern Andes (NAS), Peruvian–Atacaman Deserts (PAD), Central Andes (CAS), Amazonian–Orinocan Lowlands (AOL), Eastern Highlands (EHL), and Gran Chaco (GCH).

Spatial cross-validation results (Figure 4) indicated that the fusion model achieves consistently high skill across observational variants. Performance metrics, including the refined index of agreement (d_r), the modified Kling–Gupta efficiency (KGE''), the Matthews correlation coefficient (MCC), and balanced accuracy ($BAcc$), demonstrated strong agreement between reconstructed and observed precipitation in both magnitude (d_r and $KGE'' > 0.5$) and occurrence (MCC and $BAcc > 0.5$). Temporally complete datasets (obs_bc and hmg_obs_bc) generally exhibited slightly higher median performance, reflecting the benefits of data continuity and consistency for model training and evaluation. Stratification by ENSO conditions reveals only minor differences in performance across neutral, El Niño, and La Niña phases, as well as between eastern and central Pacific regimes. A slight reduction in performance was observed during El Niño in the eastern Pacific regime, indicating increased difficulty in representing more complex spatial precipitation variability under these conditions. Nevertheless, the spatial data fusion model remained largely insensitive to large-scale climate variability, maintaining consistent skill across varying atmospheric states. This behavior highlights the ability of the framework to generalize across different precipitation regimes without requiring regime-specific calibration.

Temporal cross-validation (Figure 5) further confirms the consistency of reconstruction performance across diverse climatic regions. Performance remained broadly stable across observational variants in both magnitude and occurrence, with slightly higher skill for temporally complete datasets. However, clear regional differences emerged at both ecoregion and station scales. Skill decreases from EHL to the AOL, NAS, CAS, GCH, and PAD. These patterns reflect underlying hydroclimatic and observational characteristics: regions with wetter conditions, flatter terrain, and denser station networks tend to exhibit higher performance, whereas arid regions with complex topography and sparse observations show reduced skill. For example, southern EHL, characterized by a dense station network, exhibited the highest performance across datasets, while PAD showed lower skill due to the dominance of zero-precipitation conditions typical of extremely arid environments. Despite these regional contrasts, overall performance remains moderate to high, indicating that the fusion approach is robust to variations in observational input and environmental conditions.

In addition, sensitivity analyses were conducted to assess the robustness of the reconstruction to both analogue selection and feature completeness (see SI Section 3). First, the evaluation was repeated using alternative analogue choices, including median- and worst-performing candidates. These experiments showed that reconstruction performance remains broadly consistent across different analogue selections, supporting the use of a single representative analogue while substantially reducing

the computational cost associated with large-scale cross-validation and long-term reconstructions. Second, an additional analysis was performed by repeating the reconstruction using non-gap-filled cloud-based (original) feature datasets instead of the gap-filled versions that were implemented. Results indicate that overall performance remained largely unchanged, demonstrating that the spatial data fusion model can effectively handle missing values in the predictor space without substantial degradation in skill. Together, these findings highlight the robustness of the AC-MSPR framework to both analogue choice and feature completeness, reinforcing its applicability in data-limited settings.

In summary, these results demonstrate that the spatial data fusion component of AC-MSPR effectively translates the diversity of analogue patterns into accurate and consistent precipitation reconstructions. The combination of robust spatial performance and stable temporal behavior across regions and climate conditions underscores the reliability and transferability of the framework for precipitation reconstruction in heterogeneous and data-limited environments.

2.4 Testbed application: long-term precipitation extremes and trends in Peru

To illustrate the applicability of the AC-MSPR framework for long-term climate analysis, we reconstructed daily precipitation over Peru for the period 1960–2015 using the best-analogue approach and derived a set of standard extreme precipitation indices (Figure 6). This testbed demonstrates the potential of the framework to generate spatially consistent datasets suitable for hydroclimatic assessments in heterogeneous, complex-terrain regions with sparse observational coverage.

Figure 6a shows the spatial distribution of mean values of precipitation extreme indices, including total precipitation (PRCPTOT), the simple precipitation intensity index (SDII), the 95th percentile of wet-day precipitation (P95), and consecutive dry (CDD) and wet (CWD) days. Coherent hydroclimatic patterns were evident across the region: high values of PRCPTOT, SDII, and P95 are concentrated in the eastern lowlands (AOL), while markedly lower values were observed along the western coastal region (PAD). Conversely, CDD reached its maximum in coastal and southern areas, whereas CWD was more pronounced in the eastern lowlands (AOL), northern regions (NAS), and parts of the Andes (CAS). These patterns were consistent with known large-scale gradients in moisture availability and topographic influences, indicating that the reconstruction successfully captures the dominant spatial features of regional precipitation regimes.

Trend analyses for these indices are presented in Figure 6b–c for the obs_bc and hmg_obs_bc variants, respectively. Trends are estimated using Sen's slope estimator and expressed at a decadal rate. Both variants exhibited broadly similar spatial structures in trend magnitude, particularly for frequency-based indices (CDD and CWD), whereas greater differences were observed for intensity-related indices (SDII and P95) and PRCPTOT. As expected, the homogenization procedure applied in hmg_obs_bc influences the magnitude of precipitation-related trends. While some regions showed both increasing and decreasing trends in PRCPTOT and intensity indices, frequency-based indices displayed more spatially extensive and coherent patterns, with tendencies

toward shorter dry periods or longer wet-day persistence. These results highlight the complexity and spatial heterogeneity of hydroclimatic change across the country.

The consistency of these trends across observational variants was evaluated in Figure 6d, which shows agreement in trend direction. Areas of agreement, where both datasets indicate either increasing or decreasing trends, highlighted robust signals that were less sensitive to differences in data processing within SC-PREC4SA. In contrast, regions of disagreement indicated higher uncertainty, potentially associated with sparse station coverage or sensitivity to temporal completeness and homogenization procedures. Statistically significant ($p\,value < 0.05$) agreement was observed for increasing trends in PRCPTOT and CWD across parts of PAD, CAS, and AOL, whereas significant decreasing trends were evident in northern AOL and southern CAS for intensity-related indices (SDII and P95) and CDD. Overall, these results suggest regionally varying changes, including increases in precipitation totals and wet-day persistence in some areas, alongside reductions in intensity and dry-day duration in others. Further comparison with independent datasets would help to strengthen the robustness of these findings.

Taken together, this testbed application demonstrates that AC-MSPR enables the reconstruction of long-term, spatially consistent precipitation datasets suitable for analyzing extremes and their trends. While mean conditions were consistently represented across observational variants, trend estimates exhibit greater sensitivity to data preprocessing choices, particularly for intensity-based indices. The ability to recover coherent large-scale signals while explicitly identifying regions of uncertainty from SC-PREC4SA underscores the value of the framework for climate analyses in data-limited regions and highlights the importance of accounting for observational uncertainty when assessing long-term hydroclimatic change.

3 Discussion

Our results demonstrate that the AC-MSPR framework provides a robust and flexible approach for precipitation reconstruction by integrating analogue-pattern selection with spatial data fusion. Analogue-conditioned patterns preserve physically consistent large-scale structures, while the fusion step refines these patterns using local observations, resulting in accurate and spatially coherent reconstructions. The framework is both data-adaptive and climate-sensitive, with analogue selection responding to observational characteristics and large-scale variability such as ENSO conditions. Despite this variability, consistently high performance across metrics indicates that the Pareto-based selection captures a diverse yet reliable set of precipitation states and effectively translates into stable reconstruction skill across spatial and temporal domains.

Beyond reconstruction accuracy, a key contribution of AC-MSPR lies in its ability to address structural limitations of existing precipitation datasets. Unlike many multi-source products that rely on sequential blending or model transitions, the framework provides an internally consistent reconstruction guided by analogue-conditioned information transfer. This reduces the risk of error cross-correlations associated with shared calibration datasets [18], as analogue selection relies on satellite precipitation products independent of gauge-based corrections. In addition, the unified modelling strategy avoids artificial temporal discontinuities linked to the harmonization of heterogeneous inputs [17, 19]. The analogue-based formulation further enables the transfer of information across time, allowing satellite-era observations to inform historical reconstructions and extending high-resolution precipitation information beyond the temporal availability of satellite products.

A further strength of AC-MSPR is its ability to operate consistently across spatial scales. The framework is applied both at the station level, where it reconstructs observational data, and at the gridded level, where it generates spatially continuous precipitation fields. This provides a unified alternative to conventional workflows in which station-based reconstruction and spatial interpolation are treated as separate steps. By contrast, AC-MSPR enables a generalized reconstruction strategy in which analogue-conditioned information and spatial data fusion are applied consistently from point to grid scale, leveraging satellite and other spatially continuous data sources within a single framework.

The application to precipitation extremes and trends highlights the potential of AC-MSPR for climate-relevant studies. The reconstructed fields capture coherent spatial patterns of extreme indices and reveal regionally heterogeneous trends, consistent with known hydroclimatic gradients. The use of temporally complete observational variants (obs_bc and hmg_obs_bc) is critical in this context, as it ensures temporal consistency in the resulting gridded reconstructions. In contrast, the direct use of observational datasets with temporal gaps would propagate inconsistencies into the reconstructed fields, potentially introducing artificial spatial and temporal heterogeneities [17, 19, 20]. This highlights the importance of reconstruction strategies that first ensure temporal completeness at the station level before generating spatially continuous datasets [6, 7], a process that is naturally supported within the AC-MSPR framework. At the same time, the comparison between observational variants underscores the importance of data characteristics in shaping long-term signals, with areas of

agreement indicating robust trends and areas of disagreement highlighting uncertainty [12].

Furthermore, AC-MSPR is intrinsically extensible. Additional environmental variables can be incorporated as auxiliary predictors, enabling a more complete representation of the atmospheric state and potentially improving reconstruction performance. This flexibility also allows the integration of alternative data sources, such as radar observations or high-frequency satellite products [27], enabling reconstruction at finer spatial and temporal resolutions and expanding the applicability of the framework to near-real-time and high-resolution monitoring contexts. More broadly, the framework could be adapted to reconstruct other hydroclimatic variables, extending its applicability beyond precipitation [26].

Nevertheless, several limitations should be considered. First, the framework's performance depends on the availability and representativeness of analogue patterns within the reference period, which may constrain its ability to capture rare or unprecedented events. Second, while the spatial data fusion model improves local accuracy, it remains sensitive to the quality and density of station observations, particularly in data-sparse regions. Third, although the analogue-based approach enables temporal information transfer, it assumes that similar large-scale conditions produce comparable precipitation responses, which may not fully hold under changing climate regimes. Finally, gauge undercatch correction remains an important aspect to consider, as it may influence the representation of precipitation magnitude beyond gap filling and homogenization [17, 34]. Future work could address these limitations by expanding the analogue pool, incorporating additional environmental predictors, and exploring adaptive or non-stationary analogue selection strategies.

Overall, AC-MSPR provides a unified framework that combines physical consistency, multi-source integration, and temporal flexibility for precipitation reconstruction. By leveraging analogue-conditioned information and spatial data fusion, the approach offers a scalable and adaptable solution for generating high-resolution precipitation datasets, particularly in regions where observational constraints have traditionally limited hydroclimatic analyses.

4 Methods

4.1 AC-MSPR

The Analogue-Conditioned Multi-Satellite Precipitation Reconstruction (AC-MSPR) framework is a data-driven hybrid model in which physical pattern similarity—identified through precipitation analogues—guides a flexible statistical learner to reconstruct daily precipitation at both point and gridded scales.

First, the framework identifies precipitation analogue patterns from satellite-based precipitation estimates that closely resemble the atmospheric conditions associated with the target observations. In addition to the satellite precipitation fields themselves, the method extracts analogue-derived features from complementary environmental variables, providing a richer representation of the large-scale conditions linked to the observed precipitation.

Second, the information from the satellite-precipitation analogues and their associated environmental features is integrated within a spatial data fusion model. This model leverages the combined analogue information to estimate precipitation at unobserved locations, producing spatially consistent (ensemble) reconstructions of daily precipitation.

4.1.1 Precipitation pattern analogue

Conceptually, the analogue resampling method samples meteorological fields for a historical period by selecting the most similar days from a reference period. These days—referred to as analogue days—are typically identified as those with the smallest differences between observational data in the historical period and observations in the reference period [24, 25]. In our case, however, rather than focusing solely on minimizing pointwise differences (e.g., RMSE), we aim to identify and match broader spatial patterns in the meteorological fields. Specifically, we search for satellite-derived precipitation fields (1998–2021) whose spatial structure resembles the precipitation pattern observed in the station data (1960–2015), hereafter referred to as precipitation pattern analogues.

To construct a pool of potential precipitation-pattern analogues for a given target date, the search was constrained to days with similar seasonal conditions and weather types to ensure physical plausibility. The following criteria were applied [25]:

- All dates within a moving window of ±60 days centred on the target date were included in the analogue pool.
- All weather types whose cumulative probability for the target date reached 95% were included in the analogue pool.

These constraints restricted the analogue search to meteorologically comparable situations while maintaining a sufficiently large pool of candidate days.

As described above, analogue selection was not based on minimizing RMSE but instead relied on a multi-metric similarity framework. Three complementary metrics were used: the refined index of agreement (d_r), a percentile-based refined index of agreement focusing on extreme precipitation (d_r^{p90}), and the Matthews correlation coefficient (MCC) computed for wet–dry occurrence (see Section 4.2.1 for equations).

These metrics capture different aspects of precipitation similarity. The metric d_r evaluates the overall spatial structure of precipitation, d_r^{p90} emphasizes the similarity of extreme precipitation patterns, and MCC measures the agreement in precipitation occurrence.

To prioritize pattern similarity rather than magnitude agreement, d_r and d_r^{p90} were computed using scaled precipitation values. Candidate analogues were then evaluated using a Pareto-based multi-objective approach [35, 36], in which no single metric was optimized independently. Instead, candidate days were selected from the Pareto-optimal set representing the best trade-offs among the three similarity measures. This approach enables the analogue search to prioritize precipitation structure, representation of extreme events, and wet–dry occurrence in satellite precipitation data, which is more physically meaningful for precipitation reconstruction than minimizing a single error metric such as RMSE.

Once the candidate analogue days were identified, additional analogue-derived predictors were extracted from the corresponding dates. These predictors can originate from complementary data sources, such as satellite products, reanalysis outputs, or radar observations, available over the satellite precipitation era. In this study, we specifically incorporated cloud-related features derived from satellite observations (see Section 4.3). These additional variables provide a physically consistent context for the selected analogue situations and were essential for enriching the spatial data fusion model, as they help bridge the gap between precipitation patterns and the underlying atmospheric conditions that generate them.

When multiple satellite products are used to identify precipitation-pattern analogues, the same calendar date can be selected as an analogue by more than one product. To avoid duplication and ensure a consistent analogue set, a consolidation step was applied. For each candidate date appearing across different products, a composite similarity score was computed by averaging the three analogue metrics (d_r, d_r^{p90}, and MCC). The date with the highest aggregated score was then retained as the representative analogue. This procedure ensures that each analogue contributes uniquely to the reconstruction while preserving the best overall compromise among spatial structure, extreme-event representation, and precipitation occurrence.

4.1.2 Spatial data fusion model

The spatial data fusion component integrates information from selected analogue patterns with observational data to generate a spatially continuous precipitation field. This part combines multiple sources of information—including satellite-derived precipitation and analogue-derived features—and refines local precipitation estimates by accounting for spatial dependencies between observation stations and analogue patterns.

A wide range of modeling architectures, spanning statistical, machine learning, and deep learning approaches, can be employed for spatial data fusion. In this study, we adopted an enhanced version of the SC-PREC4SA model [7, 12]. This improved approach is based on a three-dimensional, locally weighted hybrid random forest model, similar to the geographical random forests [37, 38]. Spatial similarity is defined using topographic attributes (elevation, latitude, longitude), not as direct covariates,

but to structure local weights. Predictions are driven by satellite precipitation patterns and analogue-based covariates (see Section 4.3).

Daily precipitation $Y(X)$ is modelled using a local two-stage hybrid approach, separating occurrence (classification) and intensity (regression) processes. Let $X = (x_1, x_2, \ldots, x_N)$ represent the vector of covariates, where N denotes the number of covariates. The modeling procedure is:

1. Occurrence model – probability of precipitation:

$$Y_{\text{class}}(\mathbf{X}) = \begin{cases} 1 & \text{if } f_c(\mathbf{X}) + \varepsilon_c \geq 0.5 \\ 0 & \text{if } f_c(\mathbf{X}) + \varepsilon_c < 0.5 \end{cases} \tag{1}$$

   Where $f_c(\mathbf{X}) \in [0, 1]$ is the predicted probability of a wet day, and ε_c is the classification model error.

2. Intensity model – precipitation amount:

$$Y_{\text{reg}}(\mathbf{X}) = f_r(\mathbf{X}) + \varepsilon_r \tag{2}$$

   Where $f_r(\mathbf{X}) \in \mathbb{R}_{\geq 0}$ is the predicted precipitation amount, and ε_r is the regression error term.

3. Final prediction:

$$\widehat{Y}(X) = Y_{\text{class}}(\mathbf{X}) \cdot Y_{\text{reg}}(\mathbf{X}) \tag{3}$$

The model uses 60 nearby stations with $N = 15$ covariates from satellite-derived precipitation and cloud properties. Precipitation variables include PrSat (magnitude) and PrSatB (binary dry/wet classification). Cloud-related features comprise H (cloud-top height), T (cloud-top temperature), OPD (optical depth), P (cloud-top pressure), CWP (column-integrated water path), and CF (cloud fraction). Derived engineering indices include DCI (deep–shallow structural index), DCI (dynamical/convective index), MDI (microphysical depth index), FDI (full deep convection index), OPD_eff (cloudiness-weighted optical depth), CWP_eff (cloudiness-weighted water load), and CF_gra (horizontal cloud structure index). See SI Section 1.3 for more details.

Spatial and topographic variability is accounted for via a three-dimensional distance metric combining horizontal distance and elevation, weighted using an Epanechnikov kernel:

1. Three-dimensional distance:

$$d_i = \sqrt{\left(d_i^{(2D)}\right)^2 + (\alpha \Delta z_i)^2} \tag{4}$$

Where $d_i^{(2D)}$ is the horizontal distance between the target and nearby station i, Δz_i is the elevation difference, and α is a scaling factor to make elevation comparable to horizontal distances.

2. Epanechnikov kernel:

$$w_i = \begin{cases} \frac{3}{4}\left(1 - \left(\frac{d_i}{h}\right)^2\right), & \text{if } d_i \leq h \\ 0, & d_i > h \end{cases} \tag{5}$$

with bandwidth h adaptively set as the median of positive distances:

$$h = \text{median}\left\{d_i : d_i > 0\right\} \tag{6}$$

Only observations within h contribute to predictions. Both occurrence $Y_{\text{class}}(\mathbf{X})$ and intensity $Y_{\text{reg}}(\mathbf{X})$ use these weights to compute locally weighted reference values, with α adjusting the influence of elevation.

This hybrid locally weighted framework provides a physically interpretable decomposition of precipitation into occurrence and intensity. The two-stage approach, combined with three-dimensional local weighting, allows accurate modeling of zero-inflated precipitation in complex terrain while preserving interpretability and robustness.

4.2 Experimental design

4.2.1 Analogue and spatial data fusion evaluation

The AC-MSPR framework was systematically evaluated to elucidate the mechanisms underlying its individual components. In particular, we assessed its performance under varying ENSO conditions and examined the effects of analogue-pattern similarity and spatial data fusion using a diverse set of metrics under different observational variants (see Section 4.3.1) in the Tropical South America region.

ENSO-flavour stratification

A temporal stratification was performed to sample days within the 1960–2015 period under distinct ENSO-flavour conditions. This approach was designed to assess the impact of ENSO asymmetry and diversity on precipitation, particularly in the context of analogue-pattern similarity and spatial data fusion.

To achieve this, we considered the eastern Pacific (EP) and central Pacific (CP) ENSO regimes, represented by the E-index and C-index, respectively [39]. ENSO phases were then defined following Cai et al. [40], allowing the classification of each day into El Niño, La Niña, or neutral conditions for both EP and CP regimes.

Based on this classification, 10% of days (n = 2046) were selected using a two-stage stratified random sampling procedure. First, 5% of days were randomly sampled according to the EP classification. Then, an additional 5% of days were drawn from the remaining dataset based on the CP classification. Therefore, the resulting sample preserves the overall distribution of ENSO phases while maintaining independence between EP and CP subsets. See SI Section 2.1 for more details.

Analogue-pattern evaluation

We evaluated analogue precipitation patterns by quantifying their similarity, size, frequency of occurrence, and performance analogue metrics across satellite-derived precipitation products under different observational dataset variants. To this end, we computed the following metrics:

- Jaccard index (similarity of analogues):

$$J(A, B) = \frac{|A \cap B|}{|A \cup B|} \tag{7}$$

  where A and B denote sets of dates representing analogous events. The index ranges from 0 (no overlap) to 1 (complete agreement), thereby providing a normalized measure of similarity between analogue sets.

- Size of analogue:

$$\text{Size}(A) = |A| \tag{8}$$

  which represents the total number of unique dates contained in the analogue set A, reflecting its extent.

- Frequency of analogues by satellite product:

$$p(s) = 100 \times \frac{|A^{(s)}|}{\sum_{s'=1}^{S} |A^{(s')}|} \tag{9}$$

  where $A^{(s)}$ is the set of analogue dates identified by satellite product s, and S is the total number of products ($S = 3$). This metric represents the relative contribution of each satellite product to the total number of detected analogues.

- Performance of analogue-pattern metrics by satellite product:

$$m_k(s) = \text{median}\left(M_k^{(s)}\right), \quad k \in \{d_r, d_r^{p90}, MCC\} \tag{10}$$

  where $M_k^{(s)} = \{x_{k,i}^{(s)} \mid i \in A^{(s)}\}$ denotes the set of values of metric k computed over the analogue dates identified by satellite product s. This quantity represents the performance of metric k, summarized by its median over all analogues associated with s.

Spatial data fusion evaluation

We evaluated the spatial and temporal performance of the spatial data fusion model using a leave-one-out cross-validation approach across multiple observational dataset variants. Model performance was assessed using the following metrics:

- Refined index of agreement (d_r) [41]:

$$d_r = 1 - \frac{\sum_{i=1}^{n} |p_i - \hat{y}_i|}{2 \sum_{i=1}^{n} |\hat{y}_i - \bar{y}|} \tag{11}$$

  where n is the number of observations, p_i is the predicted precipitation on day i, $\hat{y}_i$ is the observed precipitation on day i, and $\bar{y}$ is the mean of $\hat{y}_i$. The d_r ranges from -1 (no agreement) to 1 (perfect agreement).

- Modified kling-gupta efficiency (KGE'') [42]:

$$KGE'' = 1 - \sqrt{(r-1)^2 + (\alpha - 1)^2 + \beta^2} \tag{12}$$

  where r is the Spearman correlation coefficient between observations ($\hat{y}$) and estimates (p), $\alpha = \sigma_p / \sigma_{\hat{y}}$ is the variability ratio, $\beta = (\mu_p - \mu_{\hat{y}}) / \sigma_{\hat{y}}$ is the bias term, μ is the mean, and σ is the standard deviation. The range of KGE'' is from -∞ to 1, with 1 representing perfect agreement.

- Matthews correlation coefficient (MCC) [43]:

$$MCC = \frac{TP \cdot TN - FP \cdot FN}{\sqrt{(TP + FP)(TP + FN)(TN + FP)(TN + FN)}} \tag{13}$$

  where TP is the number of days correctly classified as wet (≥ 0.1 mm), TN as days correctly classified as dry (< 0.1 mm), FP as days incorrectly classified as wet, and FN as days incorrectly classified as dry. MCC ranges from -1 (total disagreement) to 1 (perfect agreement), with 0 indicating random classification.

- Balanced accuracy ($BAcc$) [44]:

$$BAcc = \frac{1}{2} \left(\frac{TP}{TP + FN} + \frac{TN}{TN + FP} \right) \tag{14}$$

  where TP, TN, FP, and FN are defined as above. $BAcc$ ranges from 0 (worst) to 1 (perfect classification), averaging sensitivity and specificity for balanced performance.

4.2.2 Grid-scale reconstruction

A representative testbed for tropical precipitation reconstruction under complex climatic and topographic conditions is provided by applying the AC-MSPR framework to Peru. This region is characterized by pronounced precipitation gradients and substantial climate variability. Using this framework, a daily gridded precipitation dataset at 0.1° was developed for the period 1960–2015. Furthermore, a suite of extreme precipitation indices was derived from the dataset to assess both mean and extreme precipitation variability and associated long-term trends. The chosen indices were total

precipitation (PRCPTOT), simple precipitation intensity index (SDII), 95th percentile value (P95), and consecutive dry (CDD) and wet (CWD) days. Trend magnitude was performed using Sen's slope estimator.

4.3 Data

4.3.1 Observational precipitation dataset

Station-based precipitation observations were used for both training and evaluation of the reconstruction framework. The data originate from national meteorological networks and public/private station archives compiled in the SC-PREC4SA [12]. SC-PREC4SA provides nine variants of observed daily precipitation for 1960–2015, spanning 7794 stations across the continent.

For this study, three target datasets were selected for Tropical South America (Peru): a quality-controlled observational (qc_obs), a gap-filled observational (obs_bc), and a homogenized, gap-filled (hmg_obs_bc) dataset, derived from 6895 (1271) stations. These datasets represent different observational variants, corresponding respectively to baseline observational realism, temporal completeness, and temporal consistency. More details on the observational dataset and study area are provided in SI Section 1.1.

4.3.2 Weather types data

A key part of the analogue approach involves selecting historical days with atmospheric conditions similar to those on the target date. To achieve this, we initially relied on previously developed daily weather types for Tropical South America [45, 46], which cover the period 1960–2021. However, these weather types were originally constructed separately for two atmospheric levels (850 hPa and 200 hPa) and were based on a deterministic (hard) classification without associated probabilities.

To address these limitations, we developed a new set of weather types by combining the classifications from the two atmospheric levels and introducing a probabilistic framework to quantify classification uncertainty [47]. The resulting scheme retained the same number of weather types (nine). In addition, each day was assigned a probability distribution across the nine types, allowing the representation of uncertainty in the classification. Details of the calculation procedure are provided in SI Section 1.2.

4.3.3 Satellital precipitation estimates

Satellite-based precipitation products were used to provide spatial information on precipitation patterns, to support the analogue selection process, and as a covariate in the spatial data fusion model. In this study, three products were employed: the Integrated Multi-satellitE Retrievals for GPM – Early Run, version 7 (IMERG-Early) [48]; the Global Satellite Mapping of Precipitation operational product, version 8 (GSMaP_NRT) [49]; and the Precipitation Estimation from Remotely Sensed Information using Artificial Neural Networks – Dynamic Infrared Rain Rate Near Real-Time (PDIR-Now) [50].

Both IMERG-Early and GSMaP_NRT are available from January 1, 1998, at a spatial resolution of 0.1°, while PDIR-Now has been available since March 1, 2000, at a spatial resolution of 0.04°. All datasets were obtained at hourly temporal resolution, aggregated to daily totals, and resampled to a common spatial resolution of 0.1°. Neither fused nor gauge-corrected product versions were used to avoid inflated metric inconsistencies between satellite estimates and station observations in the analogue scores and the spatial data fusion model.

4.3.4 Cloud-based and topographic variables

To enhance the spatial data fusion model, we incorporated cloud-related features from the Pathfinder Atmospheres Extended (PATMOS-x) Cloud Properties Climate Data Record [51, 52]. PATMOS-x provides multiple cloud-property variables derived from radiance and reflectance observations collected by several satellite missions, including the Advanced Very High Resolution Radiometer (AVHRR). The dataset offers global coverage at a spatial resolution of 0.1° and spans the period from 1979 to the present. In this study, however, we used data beginning on January 1, 1998, to ensure temporal consistency with the satellite-based precipitation products employed in our analysis. From the PATMOS-x dataset, we extracted six variables: cloud-top height (H), cloud-top temperature (T), cloud optical depth (OPD), cloud-top pressure (P), integrated cloud water path (CWP), and cloud fraction (CF).

In addition to the original variables, several physically motivated engineered indices were derived from the PATMOS-x cloud properties to capture convective structure and cloud microphysical characteristics better. These indices include the deep–shallow structural index (DSI), the dynamical/thermodynamic cloud index (DCI), the microphysical depth index (MDI), the full convection index (FDI), the cloudiness-weighted optical depth (OPD_eff), the cloudiness-weighted water load (CWP_eff), and the horizontal cloud structure index (CF_gra). These derived features aim to summarize interactions between cloud vertical structure, microphysics, and spatial organization that may be relevant for precipitation estimation. See SI Section 1.3 for calculation details.

Elevation data were obtained from the global topographic covariate dataset developed by Amatulli et al. [53]. This dataset provides a comprehensive suite of terrain-derived variables based on the 7.5 arc-second Global Multi-resolution Terrain Elevation Data (GMTED2010) at multiple spatial resolutions worldwide. In this study, we used the 1-km resolution elevation product. Geographic variables, including elevation, latitude, and longitude, were incorporated to define spatial weighting rather than as direct auxiliary predictors, thereby characterizing spatial proximity and terrain-related similarity among point stations/grid cells within the spatial data fusion framework.

Data availability

SC-PREC4SA data were obtained from its Figshare repository (https://doi.org/10.6084/m9.figshare.c.7588178.v4). IMERG-Early were retrieved

from the GES DISC portal (https://doi.org/10.5067/GPM/IMERG/3B-HH-E/07). PDIR-Now data were downloaded from the CHRS Data Portal (https://chrsdata.eng.uci.edu/). GSMaP_NRT data were accessed via the Google Earth Engine repository (https://doi.org/10.57746/EO.01gs73bkt358gfpy92y2qns5e9). PATMOS-x cloud data were likewise retrieved from the Google Earth Engine repository (https://doi.org/10.7289/V5348HCK).

Code availability

AC-MSPR implementation and application were performed in R (v4.5.0). The entire code and dataset are freely available at GitHub (https://github.com/adrHuerta/ac-mspr) and figshare [54] under the GNU General Public License v3.0.

Acknowledgements

AH acknowledges support from Swiss Government Excellence Scholarships for Foreign Scholars (ESKAS-Nr: 2023.0404). RSN is supported by grant RYC2021-034330-I funded by MCIN/AEI/10.13039/501100011033 and by "European Union NextGenerationEU/PRTR".

Author Contributions Statement

AH developed the methodology, experimental design, and dataset in consultation with RSN and SB. AH prepared the data, conducted the experiments, and drafted the initial manuscript. All authors contributed to discussions on the methodology, as well as data development and quality, and all reviewed and approved the manuscript.

Competing Interests Statement

The authors declare no competing interests.

References

[1] Madakumbura, G.D., Thackeray, C.W., Norris, J., Goldenson, N., Hall, A.: Anthropogenic influence on extreme precipitation over global land areas seen in multiple observational datasets. Nature Communications **12**(1), 3944 (2021) https://doi.org/10.1038/s41467-021-24262-x

[2] Yin, D., Li, X., Wang, F., Liu, Y., Croke, B.F., Jakeman, A.J.: Water-energy-ecosystem nexus modeling using multi-objective, non-linear programming in a regulated river: Exploring tradeoffs among environmental flows, cascaded small hydropower, and inter-basin water diversion projects. Journal of environmental management **308**, 114582 (2022) https://doi.org/10.1016/j.jenvman.2022.114582

[3] Gebrechorkos, S.H., Leyland, J., Dadson, S.J., Cohen, S., Slater, L., Wortmann, M., Ashworth, P.J., Bennett, G.L., Boothroyd, R., Cloke, H., *et al.*: Global scale evaluation of precipitation datasets for hydrological modelling. Hydrology and Earth System Sciences Discussions **2023**, 1–33 (2023) https://doi.org/10.5194/hess-28-3099-2024

[4] Su, J., Miao, C., Zwiers, F., Beck, H., Jones, P., Sun, Q., Slater, L.J., Berghuijs, W.R., Wada, Y., Rosenfeld, D., et al.: Precipitation observing network gaps limit climate change impact assessment. Nature, 1–7 (2026) https://doi.org/10.1038/s41586-026-10300-5

[5] Chen, H., Wang, T., Montzka, C., Gao, H., Guo, N., Chen, X., Vereecken, H.: Toward an improved ensemble of multi-source daily precipitation via joint machine learning classification and regression. Atmospheric Research **304**, 107385 (2024) https://doi.org/10.1016/j.atmosres.2024.107385

[6] Serrano-Notivoli, R., Beguería, S., Saz, M.Á., Longares, L.A., Luis, M.: SPREAD: a high-resolution daily gridded precipitation dataset for Spain–an extreme events frequency and intensity overview. Earth System Science Data **9**(2), 721–738 (2017) https://doi.org/10.5194/essd-9-721-2017

[7] Huerta, A., Brönnimann, S., Luis, M., Beguería, S., Serrano-Notivoli, R.: Enhancing daily precipitation reconstruction: An improved version of the reddPrec R package. Environmental Modelling & Software, 106717 (2025) https://doi.org/10.1016/j.envsoft.2025.106717

[8] Tapiador, F.J., Roca, R., Del Genio, A., Dewitte, B., Petersen, W., Zhang, F.: Is precipitation a good metric for model performance? Bulletin of the American Meteorological Society **100**(2), 223–233 (2019) https://doi.org/10.1175/BAMS-D-17-0218.1

[9] Li, R., Guilloteau, C., Kirstetter, P.-E., Foufoula-Georgiou, E.: How well does the IMERG satellite precipitation product capture the timing of precipitation events? Journal of Hydrology **620**, 129563 (2023) https://doi.org/10.1016/j.jhydrol.2023.

129563

[10] Sun, Q., Miao, C., Duan, Q., Ashouri, H., Sorooshian, S., Hsu, K.-L.: A review of global precipitation data sets: Data sources, estimation, and intercomparisons. Reviews of geophysics **56**(1), 79–107 (2018) https://doi.org/10.1002/2017RG000574

[11] Hunziker, S., Gubler, S., Calle, J., Moreno, I., Andrade, M., Velarde, F., Ticona, L., Carrasco, G., Castellón, Y., Oria, C., *et al.*: Identifying, attributing, and overcoming common data quality issues of manned station observations. International journal of climatology **37**(11), 4131–4145 (2017) https://doi.org/10.1002/joc.5037

[12] Huerta, A., Serrano-Notivoli, R., Brönnimann, S.: SC-PREC4SA: A serially complete daily precipitation dataset for South America. Scientific Data **12**(1), 1006 (2025) https://doi.org/10.1038/s41597-025-05312-1

[13] Derin, Y., Anagnostou, E., Berne, A., Borga, M., Boudevillain, B., Buytaert, W., Chang, C.-H., Chen, H., Delrieu, G., Hsu, Y.C., *et al.*: Evaluation of GPM-era global satellite precipitation products over multiple complex terrain regions. Remote Sensing **11**(24), 2936 (2019) https://doi.org/10.3390/rs11242936

[14] Tang, G., Clark, M.P., Papalexiou, S.M.: EM-Earth: the ensemble meteorological dataset for planet earth. Bulletin of the American Meteorological Society **103**(4), 996–1018 (2022) https://doi.org/10.1175/BAMS-D-21-0106.1

[15] Lyu, Y., Yong, B.: A novel Double Machine Learning strategy for producing high-precision multi-source merging precipitation estimates over the Tibetan Plateau. Water Resources Research **60**(4), 2023–035643 (2024) https://doi.org/10.1029/2023WR035643

[16] Wang, J., Li, X., Wu, R., Mu, X., Wei, J., Huang, Y., Gu, S., Yin, D., Tao, X., Xu, K.: A multi-source precipitation blending method combining hydrological model-guided precipitation adjustment and double transfer learning-based data merging. Journal of Hydrology, 135448 (2026) https://doi.org/10.1016/j.jhydrol.2026.135448

[17] Wang, X., Alharbi, R.S., Baez-Villanueva, O.M., Miralles, D.G., Ma, J., Xu, S., McCabe, M., Pappenberger, F., Dijk, A.I., McVicar, T.R., et al.: MSWEPV3: MachineLearning-Powered Global Precipitation Estimates at 0.1° Hourly Resolution (1979–Present) (2026) https://doi.org/10.48550/arXiv.2602.01436

[18] Xu, Y., Tang, G., Zhu, S., Li, L., Xiong, W., Ma, M., Wan, W.: Optimization of feature inputs in machine learning-based multi-source precipitation merging. Journal of Hydrology, 134185 (2025) https://doi.org/10.1016/j.jhydrol.2025.134185

[19] Diem, J.E.: Temporal inhomogeneities in high-resolution gridded precipitation products for the southeastern United States. Hydrology and Earth System Sciences **30**(7), 1999–2011 (2026) https://doi.org/10.5194/hess-30-1999-2026

[20] Funk, C., Peterson, P., Harrison, L., Saldivar, R., Landsfeld, M., Pedreros, D., Shukla, S., Fink, A.H., Davenport, F., Peterson, S., *et al.*: The Climate Hazards Center Infrared Precipitation with Stations, Version 3. Scientific Data (2026) https://doi.org/10.1038/s41597-026-07096-4

[21] Brönnimann, S.: From climate to weather reconstructions. PLoS climate **1**(6), 0000034 (2022) https://doi.org/10.1371/journal.pclm.0000034

[22] Zaman, T., Gutmann, E., Wang, G., Astitha, M.: Validation of the Ensemble Generalized Analog Regression Downscaling (En-GARD) Model to Downscale Near-Surface Wind Speed for the Northeast United States. Journal of Hydrometeorology **26**(1), 35–48 (2025) https://doi.org/10.1175/JHM-D-24-0075.1

[23] Hokson, J.A., Kanae, S., Hiraga, Y.: Predicting tropical cyclone rainfall through perceptual-based identification of similar atmospheric fields. Weather and Climate Extremes, 100896 (2026) https://doi.org/10.1016/j.wace.2026.100896

[24] Pfister, L., Brönnimann, S., Schwander, M., Isotta, F.A., Horton, P., Rohr, C.: Statistical reconstruction of daily precipitation and temperature fields in Switzerland back to 1864. Climate of the Past **16**(2), 663–678 (2020) https://doi.org/10.5194/cp-16-663-2020

[25] Imfeld, N., Pfister, L., Brugnara, Y., Brönnimann, S.: A 258-year-long data set of temperature and precipitation fields for Switzerland since 1763. Climate of the Past **19**(3), 703–729 (2023) https://doi.org/10.5194/cp-19-703-2023

[26] Imfeld, N., Brönnimann, S.: A daily gridded high-resolution meteorological data set for historical impact studies in Switzerland since 1763. Earth System Science Data Discussions **2025**, 1–31 (2025) https://doi.org/10.5194/essd-2025-249

[27] Debrie, E., Demaeyer, J., Vannitsem, S.: Hourly precipitation fields at 1 km resolution over Belgium from 1940 to 2016 based on the analog technique. Earth System Science Data **17**(11), 6405–6421 (2025) https://doi.org/10.5194/essd-17-6405-2025

[28] Valente, G., Bobadilla, H., El Skaf, R., Nappo, F.: Tales of twin cities: what are climate analogues good for? European Journal for Philosophy of Science **14**(3), 34 (2024) https://doi.org/10.1007/s13194-024-00597-2

[29] Sun, S., Nai, C., Pan, B., Li, W., Li, L., Li, X., Foufoula-Georgiou, E., Lin, Y.: Fusion of multi-source precipitation records via coordinate-based generative models. Nature Communications (2025) https://doi.org/10.1038/s41467-025-67987-9

[30] Chen, H., Zeng, J., Lyu, Y., Yong, B.: Multisource precipitation data fusion: Generating high-quality precipitation estimates. The Innovation Geoscience **4**(1), 100195–1 (2026) https://doi.org/10.59717/j.xinn-geo.2026.100195

[31] Condom, T., Martínez, R., Pabón, J.D., Costa, F., Pineda, L., Nieto, J.J., López, F., Villacis, M.: Climatological and hydrological observations for the South American Andes: in situ stations, satellite, and reanalysis data sets. Frontiers in Earth Science **8**, 92 (2020) https://doi.org/10.3389/feart.2020.00092

[32] Espinoza, J.C., Garreaud, R., Poveda, G., Arias, P.A., Molina-Carpio, J., Masiokas, M., Viale, M., Scaff, L.: Hydroclimate of the Andes part I: main climatic features. Frontiers in Earth Science **8**, 64 (2020) https://doi.org/10.3389/feart.2020.00064

[33] Marengo, J.A., Ambrizzi, T., Reboita, M.S., Costa, M.H., Dereczynski, C., Alves, L.M., Cunha, A.P.: Climate variability and change in tropical South America. In: Tropical Marine Environments of Brazil: Spatio-Temporal Heterogeneities and Responses to Climate Changes, pp. 15–44. Springer, ??? (2023). https://doi.org/10.1007/978-3-031-21329-8_2

[34] Buisán, S.T., Serrano-Notivoli, R., Kochendorfer, J., Bello-Millán, F.J.: Adjustment of solid precipitation during the Filomena extreme snowfall event in Spain: from observations to "true precipitation". Bulletin of the American Meteorological Society **103**(11), 2570–2578 (2022) https://doi.org/10.1175/BAMS-D-22-0012.1

[35] Ngatchou, P., Zarei, A., El-Sharkawi, A.: Pareto Multi Objective Optimization. In: Proceedings of the 13th International Conference On, Intelligent Systems Application to Power Systems, pp. 84–91 (2005). https://doi.org/10.1109/ISAP.2005.1599245

[36] Tan, C.S., Gupta, A., Ong, Y.-S., Pratama, M., Tan, P.S., Lam, S.K.: Pareto optimization with small data by learning across common objective spaces. Scientific Reports **13**(1), 7842 (2023) https://doi.org/10.1038/s41598-023-33414-6

[37] Georganos, S., Grippa, T., Niang Gadiaga, A., Linard, C., Lennert, M., Vanhuysse, S., Mboga, N., Wolff, E., Kalogirou, S.: Geographical random forests: a spatial extension of the random forest algorithm to address spatial heterogeneity in remote sensing and population modelling. Geocarto International **36**(2), 121–136 (2021) https://doi.org/10.1080/10106049.2019.1595177

[38] Georganos, S., Kalogirou, S.: A forest of forests: a spatially weighted and computationally efficient formulation of geographical random forests. ISPRS International Journal of Geo-Information **11**(9), 471 (2022) https://doi.org/10.3390/ijgi11090471

[39] Takahashi, K., Dewitte, B.: Strong and moderate nonlinear El Niño

regimes. Climate dynamics **46**(5), 1627–1645 (2016) https://doi.org/10.1007/s00382-015-2665-3

[40] Cai, W., McPhaden, M.J., Grimm, A.M., Rodrigues, R.R., Taschetto, A.S., Garreaud, R.D., Dewitte, B., Poveda, G., Ham, Y.-G., Santoso, A., *et al.*: Climate impacts of the El Niño–southern oscillation on South America. Nature Reviews Earth & Environment **1**(4), 215–231 (2020) https://doi.org/10.1038/s43017-020-0040-3

[41] Willmott, C.J., Robeson, S.M., Matsuura, K.: A refined index of model performance. International Journal of climatology **32**(13), 2088–2094 (2012) https://doi.org/10.1002/joc.2419

[42] Santos, L., Thirel, G., Perrin, C.: Pitfalls in using log-transformed flows within the KGE criterion. Hydrology and Earth System Sciences **22**(8), 4583–4591 (2018) https://doi.org/10.5194/hess-22-4583-2018

[43] Chicco, D., Jurman, G.: The Matthews correlation coefficient (MCC) should replace the ROC AUC as the standard metric for assessing binary classification. BioData Mining **16**(1), 4 (2023) https://doi.org/10.1186/s13040-023-00322-4

[44] Thölke, P., Mantilla-Ramos, Y.-J., Abdelhedi, H., Maschke, C., Dehgan, A., Harel, Y., Kemtur, A., Berrada, L.M., Sahraoui, M., Young, T., *et al.*: Class imbalance should not throw you off balance: Choosing the right classifiers and performance metrics for brain decoding with imbalanced data. NeuroImage **277**, 120253 (2023) https://doi.org/10.1016/j.neuroimage.2023.120253

[45] Espinoza, J.-C., Arias, P.A., Moron, V., Junquas, C., Segura, H., Sierra-Pérez, J.P., Wongchuig, S., Condom, T.: Recent changes in the atmospheric circulation patterns during the dry-to-wet transition season in south tropical South America (1979–2020): Impacts on precipitation and fire season. Journal of Climate **34**(22), 9025–9042 (2021) https://doi.org/10.1175/JCLI-D-21-0303.1

[46] Milla, P., Espinoza, J.-C., Gutierrez-Villarreal, R., Molina-Carpio, J., Ronchail, J., Espinoza-Romero, D., Junquas, C.: Recent changes in the dry-to-wet transition season in the Andean Altiplano and related atmospheric circulation patterns (1981–2022). Climate Dynamics **63**(1), 87 (2025) https://doi.org/10.1007/s00382-024-07578-4

[47] Delaygue, G., Brönnimann, S., Jones, P.D., Blanchet, J., Schwander, M.: Reconstruction of Lamb weather type series back to the eighteenth century. Climate Dynamics **52**(9), 6131–6148 (2019) https://doi.org/10.1007/s00382-018-4506-7

[48] Precipitation Processing System (PPS) at NASA GSFC: GPM IMERG Early Precipitation L3 Half Hourly 0.1 degree x 0.1 degree V07 [Data set]. NASA Goddard Earth Sciences Data and Information Services Center (GES DISC). Accessed: 2026-04-07 (2022). https://doi.org/10.5067/GPM/IMERG/3B-HH-E/07

[49] Kubota, T., Aonashi, K., Ushio, T., Shige, S., Takayabu, Y.N., Kachi, M., Arai, Y., Tashima, T., Masaki, T., Kawamoto, N., *et al.*: Global Satellite Mapping of Precipitation (GSMaP) products in the GPM era. In: Satellite Precipitation Measurement: Volume 1, pp. 355–373. Springer, ??? (2020). https://doi.org/10.1007/978-3-030-24568-9_20

[50] Nguyen, P., Ombadi, M., Gorooh, V.A., Shearer, E.J., Sadeghi, M., Sorooshian, S., Hsu, K., Bolvin, D., Ralph, M.F.: PERSIANN dynamic infrared–rain rate (PDIR-now): A near-real-time, quasi-global satellite precipitation dataset. Journal of hydrometeorology **21**(12), 2893–2906 (2020) https://doi.org/10.1175/JHM-D-20-0177.1

[51] Heidinger, A.K., Foster, M.J., Walther, A., Zhao, X.: The pathfinder atmospheres–extended AVHRR climate dataset. Bulletin of the American Meteorological Society **95**(6), 909–922 (2014) https://doi.org/10.1175/BAMS-D-12-00246.1

[52] Heidinger, Andrew K. and Foster, Michael J. and Walther, Andi and Zhao, Xuepeng and NOAA CDR Program: NOAA Climate Data Record (CDR) of Reflectance and Brightness Temperatures from AVHRR Pathfinder Atmospheres - Extended (PATMOS-x), Version 5.3. NOAA National Centers for Environmental Information. [indicate subset used]; Accessed: June 2025 (2014). https://doi.org/10.7289/V56W982J

[53] Amatulli, G., Domisch, S., Tuanmu, M.-N., Parmentier, B., Ranipeta, A., Malczyk, J., Jetz, W.: A suite of global, cross-scale topographic variables for environmental and biodiversity modeling. Scientific data **5**(1), 1–15 (2018) https://doi.org/10.1038/sdata.2018.40

[54] Huerta, A., Serrano-Notivoli, R., Brönnimann, S.: AC-MSPR: Analogue-Conditioned Multi-Satellite Precipitation Reconstruction. figshare (2026). https://doi.org/10.6084/m9.figshare.c.8455069 . https://figshare.com/collections/_/8455069/0

Figures

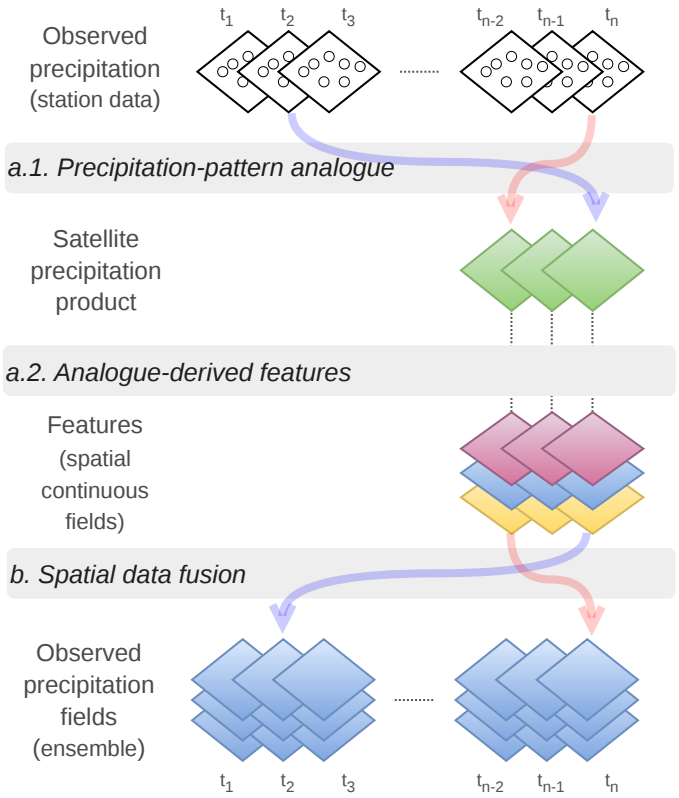

Fig. 1 Overview of the AC-MSPR framework. Schematic representation of the analogue-based multi-source precipitation reconstruction (AC-MSPR) framework. The workflow consists of two main components: (a) precipitation-pattern analogue identification, and (b) spatial data fusion. The process begins with (a.1) the identification of satellite precipitation-pattern analogues based on multi-criteria similarity metrics and the Pareto criterion, while simultaneously (a.2) extracting analogue-derived predictors, which may include spatially continuous fields from other environmental variables derived from satellite products, reanalysis, or radar data available in the same period. A spatial data fusion model (b) is then applied to reconstruct precipitation (ensemble) fields by integrating satellite precipitation observations, analogue-derived features, and station-based precipitation data. Blue and red arrows indicate the flow of information when combining past and present station observations with corresponding satellite data across temporal configurations. The framework is modular and flexible, allowing different analogue selection criteria, predictor sets, and fusion methods to be implemented consistently across spatial scales.

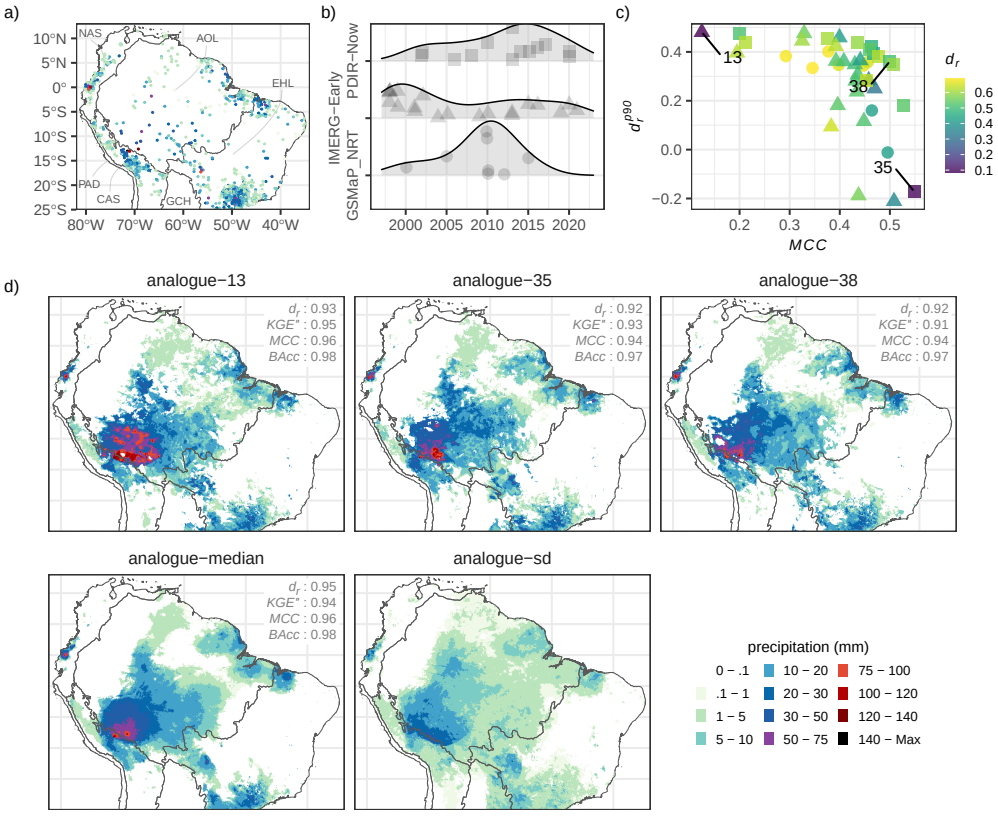

Fig. 2 Illustrative reconstruction using the AC-MSPR framework over Tropical South America. (a) Station-based precipitation from SC-PREC4SA (obs_bc - temporal completeness variant) on 10 January 1960; zero-precipitation values are omitted for clarity. (b) Temporal variability of satellite precipitation-pattern analogues selected using the Pareto-frontier criterion over the period 1998–2021 for each product (PDIR-now, IMERG-Early, and GSMaP_NRT). (c) Performance metrics of the analogue patterns shown in (b). Analogue selection is based on the refined index of agreement for all values (d_r) and extremes (90th percentile; d_r^{p90}), and the Matthews correlation coefficient (MCC) for precipitation occurrence (wet/dry). Selected analogues are identified and numbered to highlight their multi-criteria performance. (d) Reconstructed precipitation fields at 0.1° from the spatial data fusion model corresponding to the selected and numbered analogue cases in (c). Each reconstruction combines satellite analogue patterns and analogue-derived cloud-based features with observed precipitation. The ensemble median and standard deviation across analogue members are additionally shown, highlighting reconstruction uncertainty. In addition, metrics comparing gridded satellite estimates against station observations are provided, including the modified Kling–Gupta efficiency (KGE'') and balanced accuracy ($BAcc$). In panels (a) and (d), ecoregions are displayed: Northern Andes (NAS), Peruvian–Atacaman Deserts (PAD), Central Andes (CAS), Amazonian–Orinocan Lowlands (AOL), Eastern Highlands (EHL), and Gran Chaco (GCH).

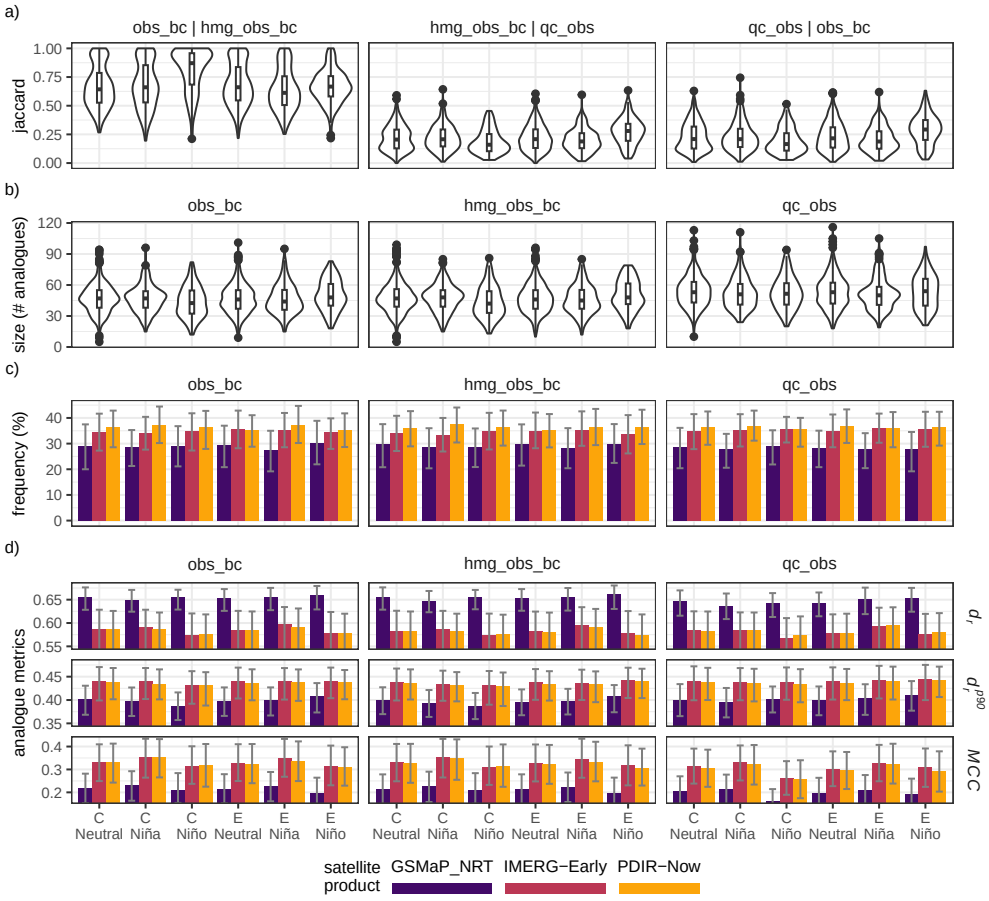

Fig. 3 Analogue-pattern selection insights under varying ENSO conditions and observational data variants over Tropical South America. (a) Similarity between analogue sets derived from different variants of the SC-PREC4SA dataset, quantified using the Jaccard index. The variants include obs_bc (temporal completeness), hmg_obs_bc (temporal consistency), and qc_obs (baseline observational realism). (b) Distribution of analogue set sizes obtained from each SC-PREC4SA variant. (c) Relative frequency (in percentage) of analogue set sizes for each satellite product (PDIR-now, IMERG-Early, and GSMaP_NRT). Each bar in (c) indicates variability represented by the interquartile range (25th–75th percentiles). (d) Mean values of analogue performance metrics for each satellite product, including the refined index of agreement for all values (d_r) and extremes (d_r^{p90}), and the Matthews correlation coefficient (MCC) for precipitation occurrence (wet/dry). All panels are stratified according to ENSO conditions, distinguishing La Niña, El Niño, and neutral phases, as well as eastern (E) and central (C) Pacific ENSO regimes.

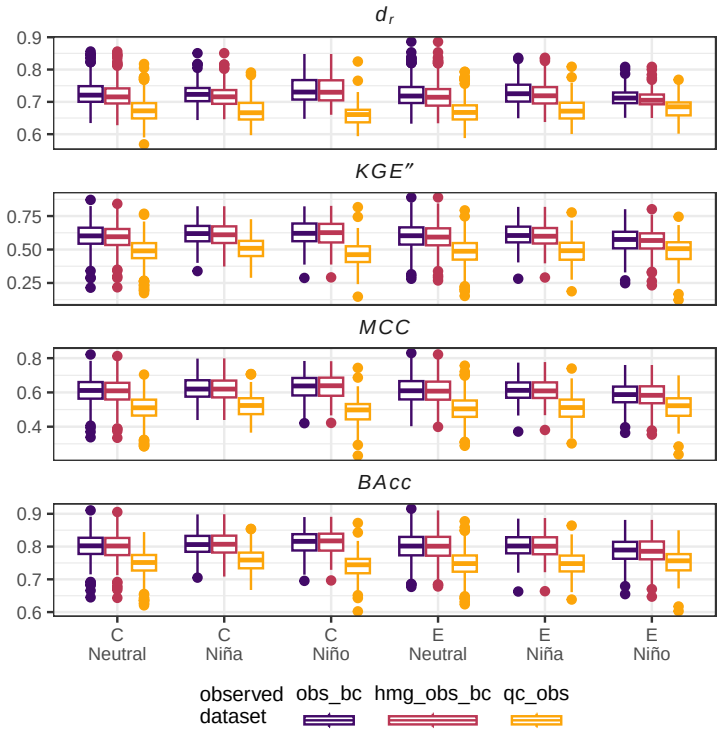

Fig. 4 Spatial data fusion insights under varying ENSO conditions and observational data variants over Tropical South America: spatial cross-validation. Box plots summarizing leave-one-out spatial cross-validation between spatial data fusion precipitation estimates and observations from the SC-PREC4SA dataset. The observational variants include obs_bc (temporal completeness), hmg_obs_bc (temporal consistency), and qc_obs (baseline observational realism). Spatial data fusion performance is evaluated using multiple metrics, including the refined index of agreement (d_r), the modified Kling–Gupta efficiency (KGE''), the Matthews correlation coefficient (MCC), and balanced accuracy ($BAcc$). All panels are stratified according to ENSO conditions, distinguishing La Niña, El Niño, and neutral phases, as well as eastern (E) and central (C) Pacific ENSO regimes.

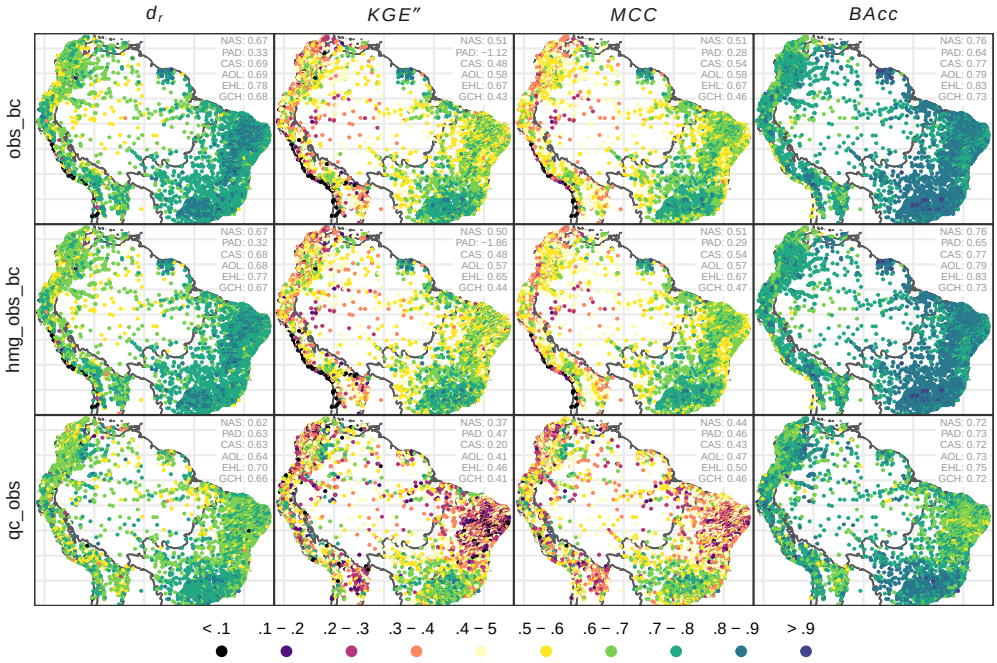

Fig. 5 Spatial data fusion insights under data variants over Tropical South America: temporal cross-validation. Leave-one-out temporal cross-validation between spatial data fusion precipitation estimates and observations from the SC-PREC4SA dataset. The observational variants include obs_bc (temporal completeness), hmg_obs_bc (temporal consistency), and qc_obs (baseline observational realism). Spatial data fusion performance is evaluated using multiple metrics, including the refined index of agreement (d_r), the modified Kling–Gupta efficiency (KGE''), the Matthews correlation coefficient (MCC), and balanced accuracy ($BAcc$). In each panel, mean metric values are shown for each ecoregion: Northern Andes (NAS), Peruvian–Atacaman Deserts (PAD), Central Andes (CAS), Amazonian–Orinocan Lowlands (AOL), Eastern Highlands (EHL), and Gran Chaco (GCH).

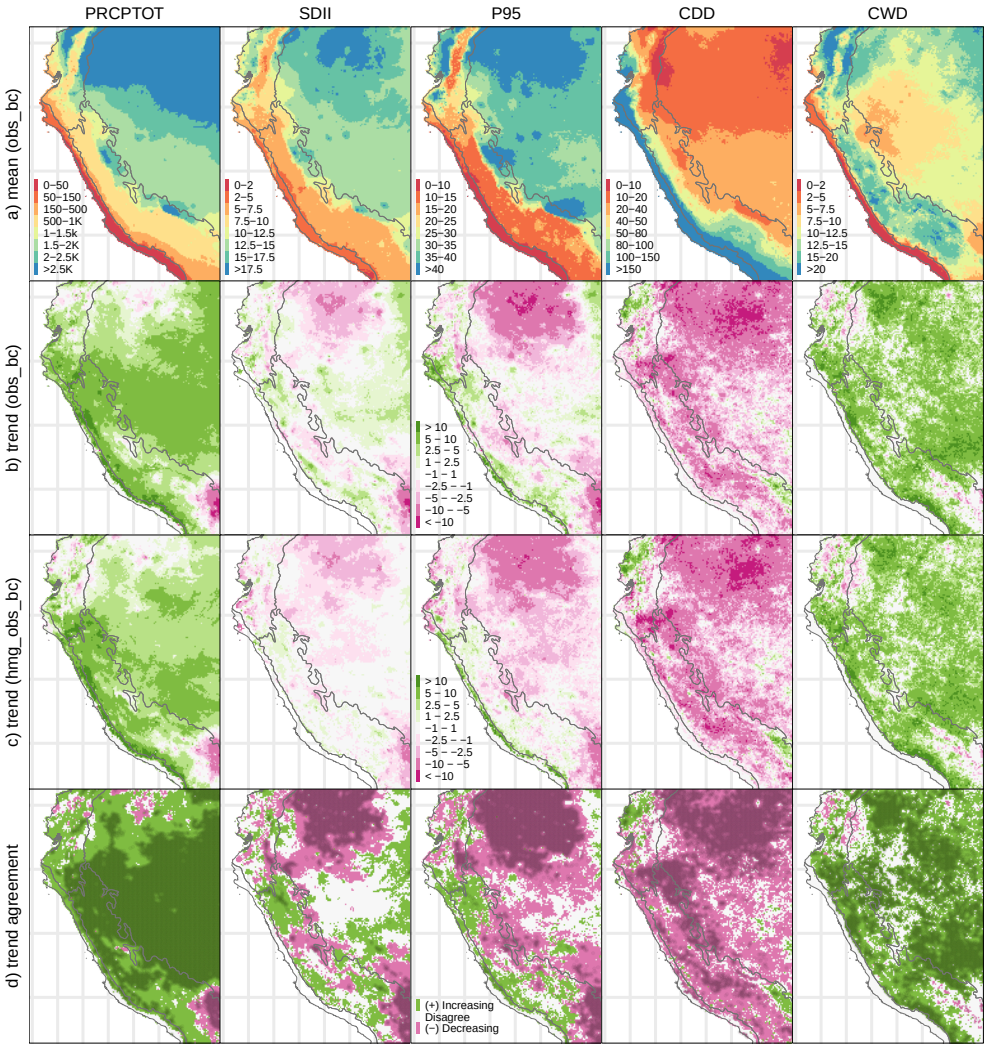

Fig. 6 Testbed application of the AC-MSPR framework in Peru. Spatial distribution at 0.1° of mean values (a) and trends (b–c) of precipitation extreme indices over Peru for the period 1960–2015, based on reconstructions using the SC-PREC4SA observational variants: obs_bc (temporal completeness) and hmg_obs_bc (temporal consistency). Extreme indices include total precipitation (PRCPTOT), the simple precipitation intensity index (SDII), the 95th percentile of wet-day precipitation (P95), and consecutive dry (CDD) and wet (CWD) days. Trend magnitudes are estimated using Sen's slope estimator and expressed at a decadal rate. In addition, (d) agreement in trend direction between datasets (b-c) is also indicated, distinguishing increasing trends (both positive), decreasing trends (both negative), and disagreement. Significant ($p\,value < 0.05$) trend agreement in (d) is displayed as darker areas.